Nano Research 2024, 17(12): 10363–10375

ISSN 1998-0124 CN 11-5974/O4
https://doi.org/10.1007/s12274-024-6989-3

Research Article

Single-particle photoluminescence connects thermal processing with heterogeneity in the trap distribution of cesium lead bromide nanocrystals

Dong Wang[1], Jie Chen[1], Dongyan Zhang[1], Dariusz M. Niedzwiedzki[2,3], Richard A. Loomis[1,4], and Bryce Sadtler[1,4] (✉)

[1] *Department of Chemistry, Washington University, St. Louis, Missouri 63130, USA*
[2] *Center for Solar Energy and Energy Storage, Washington University, St. Louis, Missouri 63130, USA*
[3] *Department of Energy, Environmental & Chemical Engineering, Washington University, St. Louis, Missouri 63130, USA*
[4] *Institute of Materials Science & Engineering, Washington University, St. Louis, Missouri 63130, USA*

Received: 3 August 2024 / **Revised:** 4 October 2024 / **Accepted:** 20 October 2024

ABSTRACT

Understanding the mechanisms of degradation in lead halide perovskite nanocrystals is critical for their future application in optoelectronic devices. We report single-particle measurements of the photoluminescence from cesium lead bromide nanocrystals coated with a silica shell ($CsPbBr_3@SiO_2$). Through correlative imaging, we quantified changes in the fluorescence intensity trajectories of the same nanocrystals before and after annealing them at different temperatures. We observe that nearly equal numbers of $CsPbBr_3@SiO_2$ nanocrystals exhibit an increase versus decrease in the amount of time they spend in an emissive state after annealing at temperatures of 70 and 100 °C. On the other hand, annealing at 120 °C produces a decrease in the on-fraction for most nanocrystals and, correspondingly, a substantial decrease in the photoluminescence intensity for a thin film annealed at this temperature. We attribute the differences in behavior among individual nanocrystals to heterogeneity in the distribution of trap states that are initially present. X-ray photoelectron, time-resolved photoluminescence, and transient absorption spectroscopies performed on thin films of $CsPbBr_3@SiO_2$ nanocrystals indicate that thermal annealing heals electron traps by passivating surface Pb ions and simultaneously creates hole traps through the formation of Pb and Cs vacancies. The relative rates of these parallel processes depend on the annealing temperature, which are important to account for when developing passivation strategies for lead halide perovskite nanocrystals in optoelectronic devices that will operate at elevated temperatures.

KEYWORDS

single-particle microscopy, photoluminescence, nanocrystals, cesium lead bromide, thermal annealing

1 Introduction

Lead halide perovskite semiconductors are of significant interest for optoelectronic applications due to their unique chemical and physical properties including tunable bandgaps, high defect tolerance, long carrier lifetimes, and low-cost processability [1–10]. However, the main challenge hindering the commercialization of these materials is their lack of stability [11–15]. Exposure to water, oxygen, heat, and light are four major causes of degradation in hybrid organic/inorganic methylammonium lead halide perovskites [16–24]. All-inorganic cesium lead halide perovskites can exhibit enhanced stability relative to their methylammonium counterparts [25, 26], but they still degrade from these environmental factors [27–41].

The encapsulation of lead halide perovskite nanocrystals and films in a polymer or silica matrix increases their resistance to water and oxygen [28–31, 42–44]. However, exposure to heat and light is inevitable in optoelectronic devices including solar cells and light-emitting diodes (LEDs). Due to the heat both absorbed from the surrounding environment and released through non-radiative relaxation of photoexcited carriers, the perovskite layer in a solar cell or LED can operate at elevated temperatures near 100 °C when not coupled with a thermal sink [45–47]. Therefore, it is important to understand how heating affects the optoelectronic properties of perovskite semiconductors.

Photoluminescence (PL) spectroscopy provides a sensitive probe of the stability of lead halide perovskites when exposed to different environments. Changes in the intensity, wavelength, and decay profiles (for time-resolved spectra) of the PL emitted by colloidal solutions or films of lead halide perovskite nanocrystals induced by exposure to controlled amounts of water, oxygen, heat, and/or light can be monitored [28–36]. However, ensemble measurements of PL spectra mask the differences in behavior among a population of nanocrystals within the sample that arise from variations in their size, shape, degree of surface passivation, and distribution of crystal defects. Thus, it can be difficult to determine the mechanism of degradation based only on the ensemble-averaged changes in PL emission.

Single-particle PL microscopy has been used to reveal heterogeneity in the chemical and photophysical properties of colloidal semiconductor nanocrystals [38–40, 48–53]. In particular, the PL intermittency (i.e., the fluctuation between

---

Address correspondence to sadtler@wustl.edu

emissive and non-emissive states) of individual semiconductor nanocrystals is highly sensitive to the presence of defect states that mediate non-radiative recombination [54–68]. For example, Boote and coworkers used single-particle PL microscopy to show that the duration and frequency of on events (i.e., when the nanocrystal is in an emissive state) for cesium lead bromide ($CsPbBr_3$) nanocrystals decreased after exposure to simulated sunlight for several hours [38]. While single-particle PL microscopy has provided new insights into the degradation mechanisms of lead perovskite halide nanocrystals due to light, water, and oxygen [38–40, 60, 61], it has not been used to examine the effect of thermal annealing on individual particles.

In this work, we used single-particle PL microscopy to investigate heterogeneity in the optical properties of $CsPbBr_3$ nanocrystals (NCs) coated with a silica (SiO_2) shell. The SiO_2 shells protect the $CsPbBr_3$ NCs from water and oxygen, enabling us to focus on how thermal annealing changes the PL properties of individual NCs. At the ensemble level, annealing films of $CsPbBr_3@SiO_2$ NCs at 100 °C or above leads to a decrease in their PL intensity. However, through correlative PL imaging of the same particles before and after thermal annealing, we observed a wide variation in the change in on-fraction among different core/shell $CsPbBr_3@SiO_2$ NCs that were subject to the same thermal treatment. Nanocrystals with initially higher off-fractions (i.e., that spent more time in a non-emissive state) were more likely to have an increase in their on-fraction after annealing, while nanocrystals with initially lower off-fractions were more likely to have a decrease in their on-fraction. Through single-particle PL measurements combined with X-ray photoelectron spectroscopy, time-resolved PL spectroscopy, and transient absorption spectroscopy performed on films of $CsPbBr_3@SiO_2$ NCs, we determine that the annealing temperature controls the balance between the healing of initial trap states and the creation of new ones.

2 Experimental

2.1 Materials

The following chemicals were used as received: cesium bromide (CsBr, 99.999%, Millipore Sigma Inc.), lead(II) bromide ($PbBr_2$, ≥ 98%, Alfa Aesar), oleic acid ($C_{18}H_{34}O_2$, 90%, Millipore Sigma Inc.), oleylamine ($C_{18}H_{37}N$, 70%, Millipore Sigma Inc.), hexane (C_6H_{14}, anhydrous, 95%, Millipore Sigma Inc.), 1-octadecene (ODE, $C_{18}H_{36}$, tech. 90%, Alfa Aesar), toluene ($C_6H_5CH_3$, anhydrous, 99.8%, Millipore Sigma Inc.), aqueous ammonia solution (NH_4OH, 28%–30%, Millipore Sigma Inc.), tetramethyl orthosilicate (TMOS, $SiC_4H_{12}O_4$, 99%, Millipore Sigma Inc.), tetraethyl orthosilicate ($SiC_8H_{20}O_4$, 99%, Millipore Sigma, Inc.), isopropanol (C_3H_8O, 99.9%, Millipore Sigma, Inc.), and N,N-dimethylformamide (DMF, C_3H_7NO, anhydrous, 99.8%, Millipore Sigma Inc.).

2.2 Synthesis of $CsPbBr_3$ and $CsPbBr_3@SiO_2$ nanocrystals

The method reported by Zhong et al. was adapted to synthesize the $CsPbBr_3$ NCs coated with SiO_2 shells (i.e., $CsPbBr_3@SiO_2$) [28]. We modified the reaction temperature and time to reduce the aggregation of the $CsPbBr_3@SiO_2$ NCs during the synthesis. For both the synthesis of uncoated $CsPbBr_3$ NCs and core/shell $CsPbBr_3@SiO_2$ NCs, two 50-mL, round-bottom flasks were connected to a Schlenk line and are referred to as Flask (I) and Flask (II) below. Flask (I) was used to prepare the perovskite precursor, and Flask (II) was used to grow the SiO_2 shell. The solutions in both flasks were stirred vigorously throughout the reaction using magnetic stirring.

In Flask (I), 146.8 mg of $PbBr_2$ and 85.1 mg of CsBr were mixed with 0.6 mL of oleylamine, 1.8 mL of oleic acid, and 10 mL of DMF. Flask (I) was evacuated and purged with Ar gas three times to remove oxygen. The flask was then heated to 90 °C under Ar for 1 h. After a clear solution formed, Flask (I) was allowed to cool to 40 °C under Ar. For the $CsPbBr_3@SiO_2$ NCs, 5 μL of TMOS was diluted in 10 mL of toluene and added to Flask (II). For the uncoated $CsPbBr_3@SiO_2$ NCs, toluene without TMOS was added, which is the only step that differed. Flask (II) was evacuated and purged with Ar gas three times to remove oxygen. The flask was then heated to 35 °C under Ar.

The $CsPbBr_3$ NCs and SiO_2 shells were grown simultaneously. First, 200 μL of an aqueous solution of ammonia (~ 2.9%, diluted from ~ 29% with ultrapure water from a GenPure Pro purification system) was injected into Flask (I). Then, 200 μL of the perovskite precursor solution from Flask (I) was swiftly injected into Flask (II) under vigorous stirring (i.e., 500 rpm). After 10 s, the stirring rate was reduced to 180 rpm and kept at this rate for 30 min. Finally, the resulting colloidal solution that formed in Flask (II) was collected and centrifuged at 9000 rpm for 5 min. The supernatant and the precipitate were then separated. The precipitate was redispersed in 2 mL of toluene, stored in a nitrogen-filled glovebox, and used to prepare thin films of the nanocrystals for characterization by X-ray diffraction (XRD), X-ray photoelectron spectroscopy (XPS), time-resolved PL spectroscopy, and transient absorption (TA) spectroscopy (as greater amounts of material are needed for these methods). The supernatant was also stored in a glovebox and used for single-particle PL microscopy and transmission electron microscopy. Absorption and PL spectra of solutions of the precipitate and supernatant are shown in Fig. S1 in the Electronic Supplementary Material (ESM).

2.3 Single-particle photoluminescence microscopy

Single-particle PL microscopy was performed using a Nikon N-STORM microscopy system consisting of a Nikon Ti-E motorized inverted optical microscope and a Nikon CFI-6-APO TIRF 100 × oil-immersion objective lens with a numerical aperture of 1.49 and a working distance of 210 μm. A white light-emitting diode (X-cite 120 LED) was used as the excitation source. An Andor iXon 897 electron-multiplying CCD camera with single-photon sensitivity (512 × 512, 16 μm pixels, > 90% quantum efficiency) was used to detect the PL signals. The exposure time of the camera during PL imaging was set to 20 ms.

Each sample was prepared in two steps. In the first step, SiO_2 microspheres (see the ESM for details of their synthesis) were dispersed in water at a concentration of 1 $mg \cdot mL^{-1}$ and spin coated onto a 25-mm round glass coverslip at 3600 rpm. The coverslip was annealed at 100 °C for 10 min in air and allowed to cool to room temperature. In the second step, the supernatant solution of $CsPbBr_3@SiO_2$ NCs was diluted with toluene by a factor of 200 and spin coated onto the coverslip at 3600 rpm.

After spin coating, the coverslip was assembled into a flow cell chamber (Chamlide CF-T). To provide an environment of N_2 in the flow cell during PL microscopy, N_2 gas was flowed into the cell using a syringe pump at a rate of 20 $mL \cdot h^{-1}$ starting 5 min prior to the measurement and continuously throughout the measurement. Prior to PL imaging, a brightfield image was taken to record the positions of the SiO_2 microspheres. The same area was then imaged under PL mode. To record the PL intensity trajectories of the $CsPbBr_3@SiO_2$ NCs, a green filter set (Chroma #49002-ET-EGFP, excitation window: 450–490 nm, emission window: 500–540 nm) was used. The light intensity at the focal plane was ~ 49 $\mu W \cdot cm^{-2}$. After initial imaging, the flow cell was transferred into a glovebox and annealed at the desired temperature. After annealing, the previously imaged area could be relocated based on the positions of the SiO_2 microspheres in brightfield mode. In this way, the PL intensity trajectories of the same $CsPbBr_3@SiO_2$ NCs were recorded before and after annealing.

2.4 Transmission electron microscopy (TEM)

TEM images were acquired by using a JEOL 2100F TEM operated at an acceleration voltage of 200 kV. The preparation of all TEM samples was performed in a glovebox. The supernatant solution of $CsPbBr_3$ or $CsPbBr_3@SiO_2$ NCs was drop cast onto a copper TEM grid and dried at room temperature. Annealing was done by heating the TEM grid on a hot plate in the glovebox at 100 °C for 10 min. To minimize exposure of the samples to air and moisture, the TEM grids were transported to the microscope in a nitrogen-filled plastic box sealed with parafilm.

2.5 X-ray photoelectron spectroscopy

X-ray photoelectron spectroscopy was performed using a Physical Electronics 5000 VersaProbe II Scanning ESCA (XPS) Microprobe system with a base pressure below 10^{-9} Torr. The $CsPbBr_3@SiO_2$ samples were prepared by drop casting 200 μL of the precipitate solution onto a single-crystal silicon substrate with the (111) orientation in a glovebox. The unannealed sample was left to dry at room temperature, while the annealed samples were heated to either 100 or 120 °C on a hotplate for 10 min in the glovebox. XPS data were acquired using the 1486.6 eV line from a Al Kα source at 150 W with a multichannel detector set to a pass energy of 23.5 eV for the high-resolution scans. The peak positions in the binding-energy regions for Cs 3d, Pb 4f, Br 3d, and O 1s photoelectrons were calibrated based on the C 1s peak at 284.8 eV. Peaks in the X-ray photoelectron spectra were fit with Gaussian functions using Origin software to determine their binding energies and relative areas.

2.6 Photoluminescence spectroscopy

PL spectra of colloidal solutions of the perovskite NCs were measured using a Cary Eclipse fluorescence spectrophotometer. The scan rate was set to medium, and the step size was 1 nm. To collect PL spectra of colloidal solutions of the $CsPbBr@SiO_2$ NCs and uncoated $CsPbBr_3$ NCs, 0.5 mL of the supernatant solution of each sample and 2 mL of toluene were added to a quartz cuvette. The two samples were then further diluted with toluene to have the same absorbance value of 0.4 at 400 nm. The PL spectra were collected using an excitation wavelength of 400 nm.

PL spectra of films of $CsPbBr_3@SiO_2$ NCs were collected using a Horiba Nanolog spectrofluorometer. Films of $CsPbBr_3@SiO_2$ NCs were prepared by drop casting the NC precipitate solution onto a coverslip in a glovebox. The unannealed sample was dried at room temperature, while the annealed sample was heated to 100 °C on a hotplate for 10 min in a glovebox. An excitation wavelength of 400 nm, a slit width of 3 nm, and an integration time of 0.5 s were used for collecting PL spectra of films of $CsPbBr_3@SiO_2$ NCs.

2.7 UV–visible (UV–Vis) absorption spectroscopy

Absorption spectra of colloidal solutions of the perovskite NCs in the ultraviolet and visible regions were collected using a Cary 60 UV–Vis spectrophotometer. Absorption spectra of films of $CsPbBr_3@SiO_2$ NCs were collected using a Lambda 950 UV/Vis spectrophotometer. The same samples used for collecting the PL spectra (both colloidal solutions and films on a coverslip) were used for the absorption measurements.

2.8 Time-resolved photoluminescence spectroscopy

For the films of $CsPbBr_3@SiO_2$ NCs characterized by time-resolved PL spectroscopy, steady-state extinction spectra were first recorded with a Shimadzu UV-1800 spectrophotometer in transmittance mode. Steady-state PL spectra were recorded using a Shimadzu RF-6000 spectrofluorometer. The spectra were measured upon excitation at 410 nm with excitation and emission bandwidths of 5 nm and a 455 nm long-pass glass filter at the detector entrance.

Time-resolved PL decay traces were then recorded using a time-correlated single-photon counting (TCSPC) setup consisting of standalone Simple-Tau 130 system from Becker&Hickl (Germany) equipped with a PMC-100-20 detector (GaAs version) with < 200 ps full width at half maximum (FWHM) of the instrument response function, PHD-400—high speed Si pin photodiode as the triggering module and a motorized Oriel Cornerstone 130 1/8 m monochromator with manually controlled, micrometer adjustable entrance and exit slits, 1200 lines·mm^{-1} grating blazed at 750 nm and manual filter wheel. Excitation pulses (410 nm) were produced by an Inspire100, an ultrafast optical parametric oscillator (OPO) (Spectra-Physics) pumped with a Mai-Tai, an ultrafast Ti:Sapphire laser, generating ~ 90 fs laser pulses at 820 nm with a frequency of 80 MHz. The repetition rate of the excitation (410 nm) was set to 400 kHz (2.5 ms between excitation pulses). To avoid polarization effects, the excitation beam was depolarized before the sample using an achromatic depolarizer (DPU25, Thorlabs) and focused on the sample in a circular spot of ~ 1 mm diameter with ~ 10^{10} photons cm^{-2}·pulse^{-1} (laser fluence of ~ 30 nJ·cm^{-2}). Emission was measured at a right angle to the excitation beam with a 455 nm long-pass filter placed at the entrance slit of the monochromator.

2.9 Transient absorption spectroscopy

TA spectra were collected using a Helios-EOS spectrometer (HE-VIS/NIR-3200/EOS-VIS/NIR custom system) from Ultrafast Systems. The measurement and data analysis follows a previously reported procedure [69]. The output of a Spectra Physics titanium-sapphire amplifier laser system (Spitfire PRO-HPR, 800 nm, ~ 100 fs pulses at a repetition rate of 1 kHz) was used to generate the excitation laser pulses in a Spectra Physics optical parametric amplifier (OPA-800CF-1) and the white-light (821 to 400 nm or 1.51 to 3.10 eV) probe pulses. Films of $CsPbBr_3@SiO_2$ NCs were excited at 435 nm (2.85 eV) using a low fluence of 5.8 μJ·cm^{-2}·pulse^{-1} to minimize non-linear effects and the degradation of the NCs. The overall temporal response of the TA measurements was ~ 200 fs. For each sample, five consecutive TA data sets were collected and averaged. The averaged results were chirp corrected. The TA decay profiles for t > 4 ps, after the carriers relaxed to the band-edge states, were fit to a sum of three exponential decays.

3 Results and discussion

We first characterized the structural properties of uncoated $CsPbBr_3$ and core/shell $CsPbBr_3@SiO_2$ NCs. XRD patterns indicated that both the $CsPbBr_3@SiO_2$ and $CsPbBr_3$ NCs possessed the orthorhombic perovskite phase of $CsPbBr_3$ (see Fig. S2 in the ESM). TEM images of both types of NCs are shown in Fig. 1. The as-synthesized $CsPbBr_3@SiO_2$ NCs possessed shells that were spherical in shape with an average diameter of 37.5 ± 4.1 nm (from 50 measurements, see Fig. S3(c) in the ESM). The size and shape of the $CsPbBr_3$ cores varied, and empty SiO_2 shells were occasionally observed along with the core/shell NCs. The longest axis of the $CsPbBr_3$ cores had an average value of 16.7 ± 4.1 nm, while the shortest axis had an average value of 14.6 ± 3.0 nm (Figs. S3(a) and S3(b) in the ESM). The irregular shapes of the $CsPbBr_3$ cores observed for the $CsPbBr_3@SiO_2$ NCs are consistent with etching of the nanocrystals by water, ammonia,

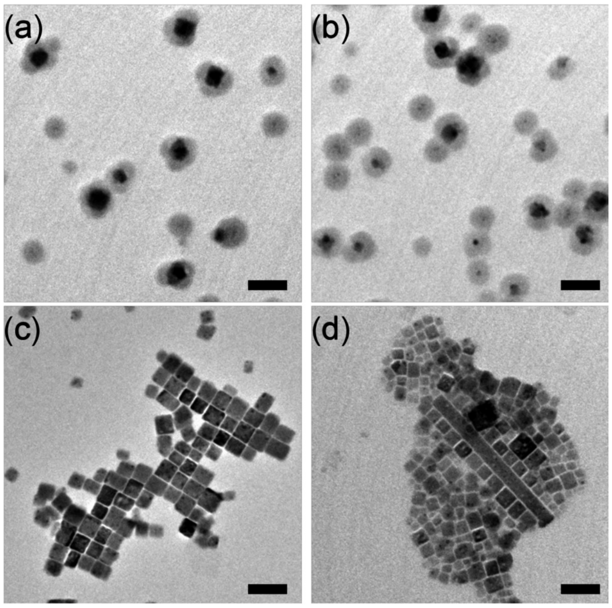

Figure 1 TEM images of (a) core/shell $CsPbBr_3@SiO_2$ NCs before annealing, (b) $CsPbBr_3@SiO_2$ NCs after annealing the sample on the TEM grid at 100 °C for 10 min in a N_2-filled glovebox, (c) uncoated $CsPbBr_3$ NCs before annealing, and (d) $CsPbBr_3$ NCs after annealing at 100 °C for 10 min in a glovebox. The scale bars are 50 nm for all images.

and TMOS during the shell growth step [28]. The uncoated $CsPbBr_3$ NCs were square in shape with average edge lengths of 18.8 ± 1.9 nm (from 50 measurements, see Fig. S3(d) in the ESM).

The emission and absorption spectra of $CsPbBr_3@SiO_2$ and $CsPbBr_3$ NCs are shown in Fig. 2. The emission maxima of the $CsPbBr_3@SiO_2$ and $CsPbBr_3$ NCs are 498 nm (2.49 eV) and 505 nm (2.45 eV), respectively. The full width at half maximum (FWHM) of the emission peaks are 0.14 eV for the $CsPbBr_3@SiO_2$ NCs and 0.15 eV for the uncoated $CsPbBr_3$ NCs. As the lateral dimensions of the $CsPbBr_3$ NCs (imaged as two-dimensional projections by TEM) are greater than the Bohr exciton diameter of $CsPbBr_3$, the shifts in the optical spectra to higher energies relative to the bulk optical band gap of $CsPbBr_3$ (~ 2.34 eV) [70] indicate that the uncoated NCs have a platelet shape (due to their orthorhombic crystal structure) with a thickness that leads to weak quantum confinement. The maximum of the lowest-energy absorption peak is 485 nm (2.56 eV) for both samples (as determined from taking the second derivative of the absorption spectra, Fig. S4(a) in the ESM). The absorption spectrum of the $CsPbBr_3@SiO_2$ NCs shows more pronounced tailing at longer wavelengths relative to the uncoated $CsPbBr_3$ NCs, which indicates the presence of optically active traps within the band gap of $CsPbBr_3$ [71]. Such traps states would also lower the PL efficiency at longer wavelengths, consistent with the differences in PL maxima between the core/shell and uncoated NCs (Fig. 2 and Fig. S4(b) in the ESM). The integrated emission intensity of the $CsPbBr_3@SiO_2$ NCs was 1.75 times the value of the uncoated $CsPbBr_3$ NCs (for solutions with the same absorbance at the excitation wavelength of 400 nm), suggesting that the $CsPbBr_3@SiO_2$ NCs have a higher overall photoluminescence quantum yield (PLQY). We attribute the difference in PLQY to the effect of the SiO_2 shell. Previous reports have shown that non-epitaxial SiO_2 shells around $CsPbBr_3$ cores can not only protect the NCs from degradation induced by H_2O and O_2, but also passivate surface defects [29–31].

We used XRD and electron microscopy to characterize potential changes to the structure and morphology of the $CsPbBr_3@SiO_2$ and $CsPbBr_3$ NCs after thermal annealing. Both the core/shell and the uncoated NCs were annealed at 100 °C for 10 min in a nitrogen-filled glovebox on a silicon substrate used to measure their XRD patterns. There were no apparent changes in the XRD patterns indicating that the crystal structure for both the uncoated $CsPbBr_3$ and core/shell $CsPbBr_3@SiO_2$ NCs did not change after this thermal treatment (Fig. S2 in the ESM). TEM images show that the uncoated $CsPbBr_3$ NCs underwent oriented attachment after annealing to form larger particles (Fig. 1(d)). The $CsPbBr_3@SiO_2$ NCs were protected from aggregation by the SiO_2 shells (Fig. 1(b)). Thus, thermal annealing at 100 °C does not noticeably change the morphology or structure of the $CsPbBr_3@SiO_2$ NCs.

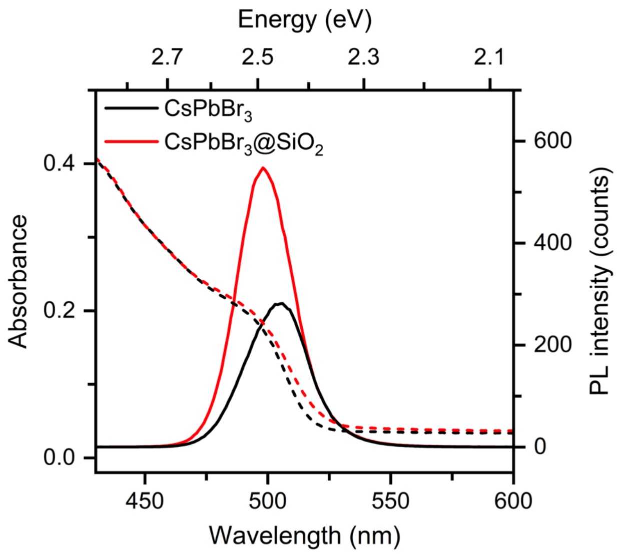

Figure 2 PL (solid lines) and UV–Vis absorption (dashed lines) spectra of core/shell $CsPbBr_3@SiO_2$ NCs (red) and uncoated $CsPbBr_3$ NCs (black) dispersed in toluene.

To compare the distribution of oxidation states in the $CsPbBr_3@SiO_2$ NCs, X-ray photoelectron spectra were measured on samples before annealing and after annealing at 100 °C and 120 °C. The spectra and fitting of peaks for Cs 3d and Pb 4f electrons are plotted in Fig. 3. The corresponding peak positions and their relative areas are summarized in Table S1 in the ESM. Spectra in the binding energy region of Cs 3d electrons were fit to either two or three peaks for each value of angular momentum (Fig. 3(a)). The primary peaks at 738.2 eV (Cs $3d_{3/2}$) and 724.2 eV (Cs $3d_{5/2}$) correspond to Cs within the $CsPbBr_3$ lattice [50, 72]. We attribute the shoulder peaks at lower binding energies of 737 eV (Cs $3d_{3/2}$) and 723 eV (Cs $3d_{5/2}$) to Cs in a lower oxidation state than in the $CsPbBr_3$ lattice. After annealing, we also observed new shoulder peaks at higher binding energies of 739 eV (Cs $3d_{3/2}$) and 725 eV (Cs $3d_{5/2}$), which we attribute to Cs in a higher oxidation state than in the $CsPbBr_3$ lattice. The primary peaks had relative areas near 82% for the unannealed film of $CsPbBr_3@SiO_2$ NCs, but the relative areas decreased to near 72% for the films annealed at both 100 and 120 °C. The relative areas of the shoulder peaks at lower binding energies were near 18% in the unannealed film but decreased to 8% for the annealed films. The new peaks at higher binding energies only appeared in films annealed at 100 and 120 °C. The relative areas of these peaks were near 20% at both annealing temperatures. Thus, thermal annealing increases the average oxidation state of Cs in the samples.

Spectra in the binding energy region of Pb 4f electrons were fit to three peaks for each value of angular momentum (Fig. 3(b)). The primary peaks at 143.1 eV (Pb $4f_{5/2}$) and 138.2 eV (Pb $4f_{7/2}$) correspond to the Pb within the $CsPbBr_3$ lattice [50, 72]. Shoulder peaks at lower binding energies of 142 eV (Pb $4f_{5/2}$) and 137 eV (Pb $4f_{7/2}$) are attributed to Pb in a lower oxidation state than in the $CsPbBr_3$ lattice. Shoulder peaks at higher binding energies of

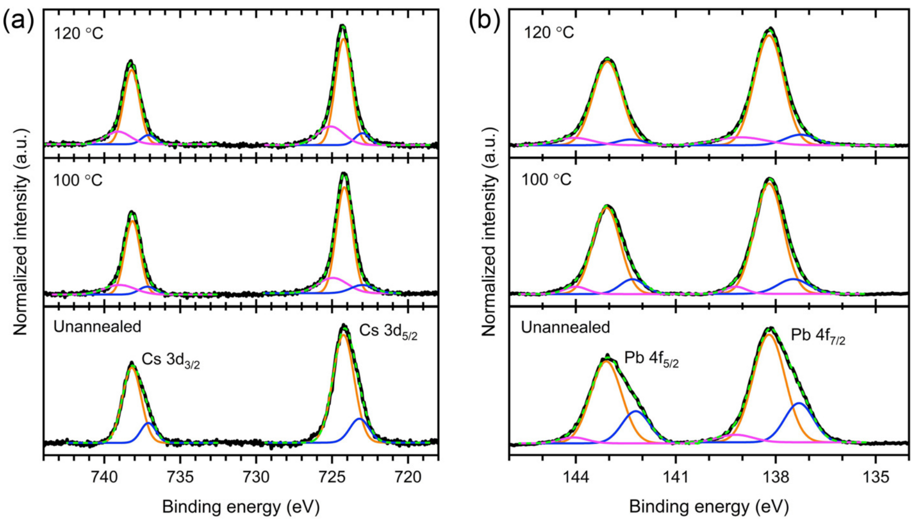

Figure 3 X-ray photoelectron spectra showing the binding energy regions for (a) Cs 3d and (b) Pb 4f electrons. Samples of $CsPbBr_3@SiO_2$ NCs before annealing, after annealing at 100 °C, and after annealing at 120 °C are shown from the bottom to top in each panel. The experimental spectra are shown in black traces. The deconvoluted peaks are shown in orange, blue, and magenta lines. The sums of fitting each set of peaks are shown as dashed green lines.

144 eV (Pb $4f_{5/2}$) and 139 eV (Pb $4f_{7/2}$) are attributed to Pb in a higher oxidation state than in the $CsPbBr_3$ lattice. The relative areas of the primary peaks increased from 72% before annealing to above 80% after annealing at both temperatures. The relative areas of the shoulder peaks at lower binding energies decreased from near 23% to 12% after annealing at 100 °C. The relative areas of these peaks further decreased to between 6% and 10% when increasing the annealing temperature to 120 °C. On the other hand, the relative areas of the shoulder peaks at higher binding energies increased from between 4% and 6% for the unannealed film and the film annealed at 100 °C to 10% for the film annealed at 120 °C. XPS in the regions of Br 3d and O 1s electrons are shown in Fig. S5 in the ESM. Similar to the observations for the Cs and Pb spectra, thermal annealing led to a reduction of the component in the Br 3d spectra with a more negative oxidation state than Br in the $CsPbBr_3$ lattice. However, we did not observe any changes in the O 1s spectra.

We next investigated the stability of the $CsPbBr_3@SiO_2$ NCs against water and oxygen. As previous reports have shown, heat is not the only factor that can promote degradation of $CsPbBr_3$ NCs [27–41]. To understand the influence of thermal annealing, other factors that can induce degradation first need to be minimized. Using PL microscopy, we observed that the stability of the core/shell $CsPbBr_3@SiO_2$ NCs was enhanced compared to $CsPbBr_3$ NCs without a SiO_2 shell. The light used to excite the NCs (i.e., 450–490 nm from an LED source) was kept at a low intensity (i.e., ~ 49 μW·cm^{-2}) to minimize photoinduced changes to the NCs. Single-particle PL intensity trajectories of $CsPbBr_3@SiO_2$ NCs were measured in a flow cell exposed to either air or N_2. For comparison, we also measured the PL intensity of uncoated $CsPbBr_3$ NCs in air.

The integrated PL intensity trajectories over the entire microscope field-of-view (containing around 200 single NCs for each sample) are shown in Fig. 4. The intensity of uncoated $CsPbBr_3$ NCs dropped quickly during the measurement. Nearly all the NCs went dark after 200 s of continuous illumination in air. Meanwhile, the integrated PL intensity of the $CsPbBr_3@SiO_2$ NCs after 400 s of continuous illumination in air maintained 75% of its original value. For the measurement in N_2, the integrated PL intensity of the $CsPbBr_3@SiO_2$ NCs after 400 s of continuous illumination was over 90% of the original intensity. Upon annealing at 70 °C, the integrated intensity of $CsPbBr_3@SiO_2$ NCs measured in N_2 did not change after 400 s of illumination while the sample annealed at 100 °C dropped by 15% (Fig. S6 in the ESM). A larger intensity drop of 50% was observed for the sample annealed at 120 °C.

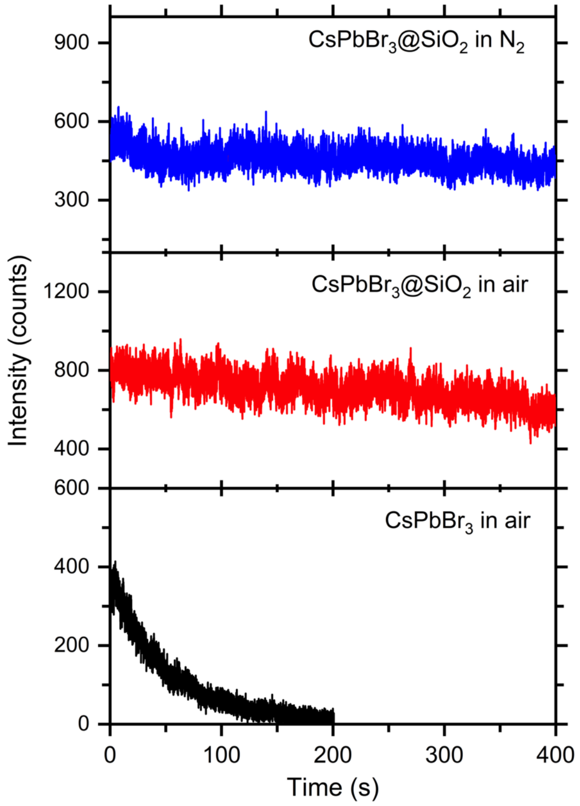

Figure 4 Integrated PL intensities over the entire microscope field-of-view for $CsPbBr_3@SiO_2$ NCs measured both in N_2 (blue, top trace) and air (red, middle trace) and uncoated $CsPbBr_3$ NCs measured in air (black, bottom trace). Differences in the initial intensity counts arise from differences in the number of NCs within the field-of-view as well as differences in the PLQY of the uncoated and core/shell NCs.

The rapid drop in PL intensity of the uncoated $CsPbBr_3$ NCs is consistent with previous reports showing that the combination of oxygen, water, and light degrade cesium lead halide NCs [28–31, 39, 40]. With the protection of a SiO_2 shell, the stability of the $CsPbBr_3$ cores was significantly improved. The minor degradation observed for the $CsPbBr_3@SiO_2$ sample measured in air might come from a portion of NCs with incomplete shell coverage. The stability was further improved when the PL intensity of the

$CsPbBr_3@SiO_2$ NCs was measured in a N_2 environment. Still, a small drop in PL intensity was observed, < 10% for the unannealed sample and 15% for the sample annealed at 100 °C, which we attribute to trap-assisted photodegradation of the $CsPbBr_3$ cores in absence of water and oxygen [36, 39, 40]. This process became more prominent for the sample annealed at 120 °C, as higher annealing temperatures appear to increase the trap density in these NCs.

To better understand the differences in stability for uncoated and core/shell $CsPbBr_3$ NCs, PL intensity trajectories of individual particles were analyzed (Fig. 5 and Fig. S7 in the ESM). Representative single-particle trajectories of uncoated $CsPbBr_3$ NCs measured in air, Fig. 5(a), show that the PL intensity of each particle progressively decreased under continuous illumination. Representative single-particle trajectories of core/shell $CsPbBr_3@SiO_2$ NCs measured in N_2 are shown in Figs. 5(b) and 5(c). The majority of the NCs (112 out of 133) did not exhibit any obvious change while recording their PL intensity for 400 s (Fig. 5(b)). Some of the NCs (11 out of 133) exhibited a small increase in their PL intensity during the experiment (see the purple and black traces in Fig. 5(b) for examples). Furthermore, a portion of $CsPbBr_3@SiO_2$ NCs (10 out of 133) exhibited more frequent and longer dark periods as time elapsed (Fig. 5(c)).

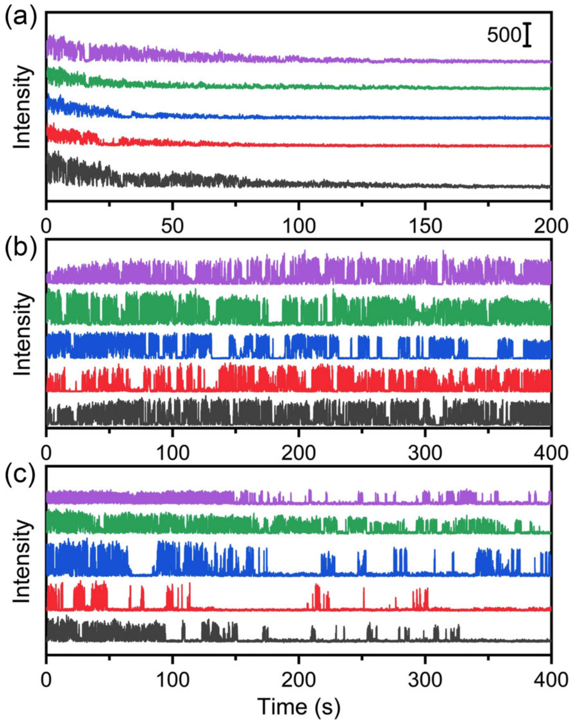

Figure 5 Representative single-particle PL intensity trajectories of (a) uncoated $CsPbBr_3$ NCs measured in air, (b) $CsPbBr_3@SiO_2$ NCs measured in N_2 that were stable during the measurement (> 90% of the total population), and (c) $CsPbBr_3@SiO_2$ NCs measured in N_2 that show an increase in their off-fraction over time (< 8% of the total population). The vertical intensity scale of 500 counts in panel (a) applies to the trajectories in all three panels.

Single-particle measurements indicate that different degradation pathways are responsible for changes in PL trajectories of uncoated and core/shell $CsPbBr_3$ nanocrystals. The steady decrease in PL intensity for uncoated $CsPbBr_3$ NCs measured in air is consistent with photochemical oxidation from exposure to air during illumination [39, 40, 73]. For $CsPbBr_3@SiO_2$ NCs measured in N_2, the $CsPbBr_3$ cores are protected from photochemical oxidation. Therefore, the PL intensities of the bright state remain constant for the majority of the core/shell NCs. The small increase in PL intensity for some of the $CsPbBr_3@SiO_2$ NCs (8%) under irradiation may arise from photobrightening where trap states become filled and thus no longer contribute to non-radiative recombination [74, 75]. However, prolonged irradiation can also create new defects in the NCs that act as non-radiative recombination centers [36, 39, 40] such that the off state becomes more prominent over time. Less than 8% of the $CsPbBr_3@SiO_2$ NCs imaged showed this behavior (see examples in Fig. 5(c)). The rest of the NCs were stable throughout the measurement (Fig. 5(b)). Thus, through the protection of the SiO_2 shell, limiting the excitation intensity, and controlling the environment during imaging, we can minimize the effects of water, oxygen, and light on the NCs, and thus focus on the influence of thermal annealing.

We used the change in PL intermittency as a signature to study the influence of thermal annealing on individual $CsPbBr_3@SiO_2$ NCs. Photoluminescence intensity trajectories of the same NCs before and after annealing were recorded. The intensity value within each 20-ms time frame was compared to a constant threshold value of 100 counts. The time frames with PL intensities higher than this threshold are defined as “on” events, while the rest of the time frames are defined as “off” events. Since the PL intermittency is highly dependent on the distribution of trap states within the NC, we used the on-fraction, which is the percentage of on events relative to the total number of events, to characterize the trap states in individual $CsPbBr_3@SiO_2$ NCs. A large on-fraction for a NC indicates a relatively low density of trap states that mediate non-radiative recombination. The on-fractions of individual $CsPbBr_3@SiO_2$ NCs before and after annealing at 70, 100, and 120 °C are plotted in Fig. S8 in the ESM. The plots show significant heterogeneity in the behavior of individual NCs upon annealing.

The variation in on-fraction before and after annealing was calculated by subtracting the on-fraction before annealing from the on-fraction after annealing. Histograms of the on-fraction variation before and after annealing at 70, 100, and 120 °C are shown in Fig. 6. A positive variation in on-fraction indicates that annealing decreased the number of non-radiative recombination centers in the NC. The average on-fraction did not significantly change for the $CsPbBr_3@SiO_2$ samples annealed at 70 and 100 °C (decrease by 6% at 70 °C and increase by 1% at 100 °C). However, the average on-fraction decreased by 33% upon annealing at 120 °C as seen by the shift in the peak of the histogram to negative values.

At each annealing temperature, we classified the NCs into three populations based on their variation in on-fraction before and after annealing. For the sample annealed at 70 °C, a total of 314 NCs were analyzed. NCs with on-fractions below 10% were considered dark. Based on this cutoff, 11% of the NCs were initially dark but became emissive after annealing (34 out of 314, data points located close to the *y*-axis in Fig. S8(a) in the ESM). After annealing at 70 °C, 24% of the NCs were initially emissive but became dark after annealing (75 out of 314, data points close to the x-axis in Fig. S8(a) in the ESM). The rest of the NCs showed a range of variations in their on-fraction (Fig. 6(a)). The samples annealed at 100 and 120 °C were analyzed in the same way. For the sample annealed at 100 °C, a total of 389 NCs were analyzed (Fig. 6(b) and Fig. S8(b) in the ESM). After annealing, 18% of initially dark NCs became emissive (70 out of 389), while 19% of the NCs became dark (75 out of 389). The majority of the other NCs were located near the red dashed line in Fig. S8(b) in the ESM, indicating a small variation in on-fraction. For the sample annealed at 120 °C, a total of 341 NCs were analyzed (Fig. 6(c) and Fig. S8(c) in the ESM) . After annealing, 10% of the NCs became emissive (33 out of 341), while 66% of the NCs became dark (226 out of 341). The variation in on-fractions for these different populations of NCs suggest that certain types of traps are

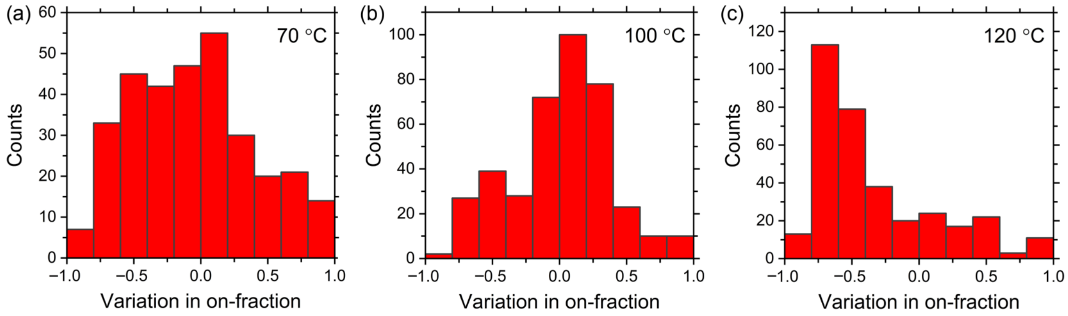

Figure 6 Histograms of the variation in on-fraction for single $CsPbBr_3@SiO_2$ NCs after annealing at (a) 70, (b) 100, and (c) 120 °C.

passivated during annealing, while new traps states are simultaneously created. Thus, while the thermal treatment did not change the overall structure or morphology of the $CsPbBr_3@SiO_2$ NCs (Fig. 1 and Fig. S2 in the ESM), it had a significant effect on the distribution of trap states.

To further understand the influence of thermal annealing on the distribution of trap states, probability distributions of on-events for individual $CsPbBr_3@SiO_2$ NCs were analyzed. The PL intermittency of a semiconductor NC can be classified based on different mechanisms of non-radiative recombination. The activation and deactivation of shallow trap states can promote non-radiative recombination of band-edge carriers. Empirically, a probability distribution that follows a linear power law, Eq. (1), indicates that blinking is dominated by non-radiative, band-edge carrier recombination (termed here as type-B blinking) [59, 67].

$$P(t) = At^{-\alpha} \tag{1}$$

where $P(t)$ is the probability of finding on events with a duration of time t, A is an empirical constant, and α is the power-law coefficient. On the other hand, photoionization of a NC leads to a long-lived trapped charge that facilitates non-radiative Auger recombination of subsequent electron–hole pairs generated while the NC is ionized [54]. A probability distribution for on events that follows a truncated power law, Eq. (2), indicates that blinking is dominated by Auger recombination (termed here as type-A blinking) [55, 59, 60].

$$P(t) = At^{-\alpha}e^{-t/t_c} \tag{2}$$

where t_c is the truncation time, and the other constants are defined as described for Eq. (1).

We focus on the sample annealed at 100 °C as it contains a similar number of NCs that became bright and dark after annealing. Among the 389 NCs in this sample, 70 NCs were initially dark before annealing (i.e., on-fractions below 10%), and 75 NCs became dark after annealing. The probability distributions of on-events could not be analyzed when the NCs were dark. Among the 319 bright NCs (i.e., on-fractions above 10%) before annealing, two different shapes of the probability distribution were observed. Similar shapes of the probability distribution were also observed among the 314 bright NCs after annealing at 100 °C (see Fig. S9 in the ESM for representative examples). Figure 7 shows representative probability distributions of on-events for two different $CsPbBr_3@SiO_2$ NCs before annealing. For the NC shown in Fig. 7(a), the event duration exhibited a linear relationship with the probability of on-events in the log–log plot (Eq. (1)). Before annealing, 90% of the NCs (286 out of 319) also exhibited a linear power-law probability distribution similar to the NC shown in Fig. 7(a). Thus, these NCs exhibited type-B blinking, dominated by shallow trap states. For the other $CsPbBr_3@SiO_2$ NC shown in Fig. 7(b), the probability distribution of on-events exhibited a truncated power law relationship (Eq. (2)). A truncation time of 0.22 s was obtained for this distribution. Before annealing, 10% of the NCs (33 out of 319) exhibited a truncated power-law probability distribution similar to the NC in Fig. 7(b), indicating that deep traps lead to photoionization during irradiation of these NCs.

The probability distributions of the 314 bright NCs after annealing at 100 °C could also be fit to one of these two power laws. Less than 8% of the NCs after annealing (25 out of 314) exhibited a truncated power-law distribution, while the rest were fit to a linear power law (see Fig. S9 in the ESM for examples). Similar to previous studies on perovskite nanocrystals [64, 66–68], the $CsPbBr_3@SiO_2$ NCs exhibit a mixture of different mechanisms for PL intermittency consistent with heterogeneity in the types of trap states present among individual NCs. However, the majority of $CsPbBr_3@SiO_2$ NCs both before and after annealing at 100 °C exhibit type-B blinking indicating that shallow traps are primarily responsible for conversion of the NCs to their non-emissive state.

Interestingly, we found that the 10% of NCs displaying type-A blinking before annealing were more likely to have a higher on-fraction after annealing at 100 °C. As shown in Fig. 8(a), most of the NCs with type-A blinking (shown in green) had a positive variation in their on-fraction after annealing. While the change in on-fraction for NCs initially exhibiting type-B blinking varied widely, the majority of these NCs had a decrease in their on-fraction after annealing (orange histogram in Fig. 8(b)). Furthermore, we compared the probability distributions of the same NCs before and after annealing. We found that the majority of NCs initially displaying type-A blinking (20 out of 33) before annealing changed to type-B blinking after annealing (see Fig. S10 in the ESM for an example). These changes in the probability distributions indicate that deep traps within the NCs (i.e., that

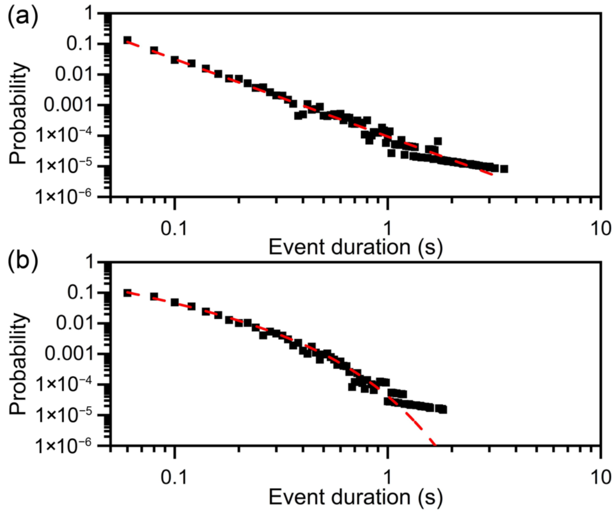

Figure 7 Representative probability distributions of on-events for two different $CsPbBr_3@SiO_2$ NCs before annealing. The probability distribution of the NC in panel (a) was fit using a linear power law (Eq. (1)), while the NC in panel (b) was fit using a truncated power law (Eq. (2)), with a truncation time of 0.22 (0.05) s.

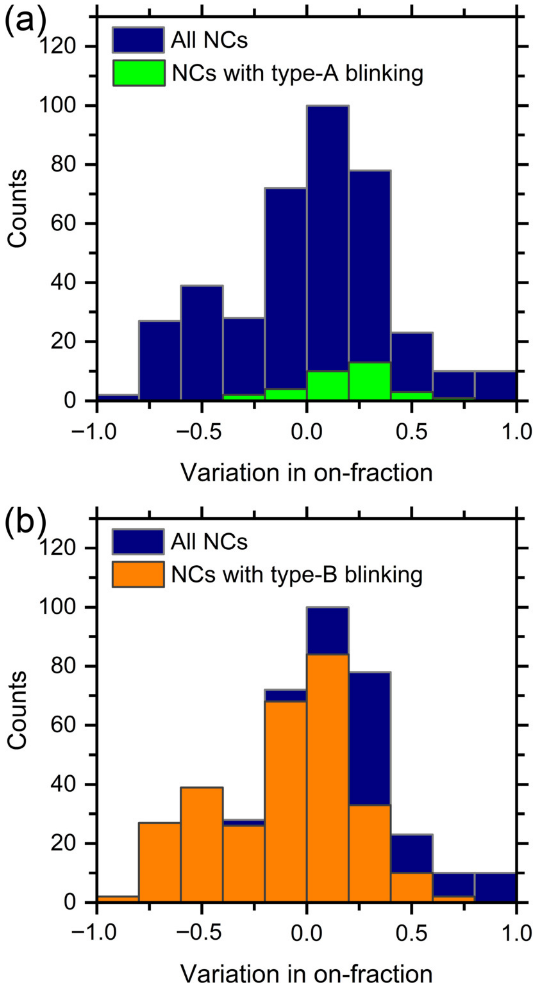

Figure 8 Histograms of the variation in on-fraction for (a) $CsPbBr_3@SiO_2$ NCs that initially exhibited type-A blinking (green) and (b) NCs that initially exhibited type-B blinking (orange). For comparison, the variation in on-fraction for the entire population of NCs (blue) annealed at 100 °C is shown in both plots. For some NCs with very high on-fractions, the probability distribution of on events could not be fit. Thus, the blue histograms include NCs that are not included in either the green or orange histograms.

promote photoionization and lead to type-A blinking) were more likely to be healed by thermal annealing at 100 °C.

We compared the probability distributions of $CsPbBr_3@SiO_2$ NCs that became brighter after annealing (i.e., a positive variation in their on-fraction) to those that became darker. A histogram of the slopes, i.e., the value of α in Eq. (1), used to fit the probability distributions of on events for the initial $CsPbBr_3@SiO_2$ NCs that exhibited type-B blinking (286 out of 319 NCs) is shown in Fig. S11 in the ESM. The slope of the power law fitting reflects the probability for on events with a long duration to occur. A greater slope indicates a higher blinking frequency and that on events with a long duration are less frequent. The distribution of initial slopes (before annealing) for NCs that exhibited an increase in their on-fraction by more than 20% after annealing at 100 °C is plotted in Fig. S11(a) in the ESM. These NCs tend to have a larger magnitude for the slope of their fit. The distribution of initial slopes for NCs that exhibited a decrease in their on-fraction by more than 20% after annealing are plotted in Fig. S11(b) in the ESM. These NCs tend to have a smaller magnitude for the slope of their fit. The differences in slopes indicate that NCs with initially higher blinking frequencies (i.e., fewer on events of long duration) were more likely to become brighter during annealing. On the other hand, NCs with initially lower blinking frequencies (i.e., more on events of long duration) were more likely to become darker after annealing.

TEM images of the $CsPbBr_3@SiO_2$ NCs (Fig. 1) show a wide distribution of sizes and shapes for the $CsPbBr_3$ cores. To investigate whether the differences in PL intermittency observed for the NCs are due to differences in their morphology, we correlated PL intensity trajectories with TEM images of the same nanocrystals. Previous reports have shown that $CsPbBr_3$ NCs are extremely sensitive to high-energy electron beams used for TEM imaging [76–78]. We found that when uncoated $CsPbBr_3$ NCs were diluted to a sufficient level for single-particle PL imaging (i.e., when each NC was separated by a distance of a few micrometers or more to avoid multiple NCs within the same diffraction-limited region), the degradation of NCs under the electron beam became more severe (relative to higher concentrations, such as in the TEM images shown in Fig. 1). The uncoated $CsPbBr_3$ NCs evaporated before an image could be recorded. However, with the protection of the SiO_2 shell, the stability of $CsPbBr_3@SiO_2$ NCs under the electron beam was significantly enhanced. Individual NCs were stable at medium magnifications for long enough to image them.

Representative TEM images of single $CsPbBr_3@SiO_2$ NCs and their PL intensity trajectories are shown in Fig. S12 in the ESM. Although we characterized NCs in which the $CsPbBr_3$ cores possessed different sizes and shapes, there was no observable correlation between the morphology of the core and the fluorescent intensity trajectory. The PL trajectories also did not show a noticeable dependence on the SiO_2 shell thickness or shell coverage. While high-resolution TEM images may provide further information on structural defects present in the NCs [79], the $CsPbBr_3@SiO_2$ NCs were not stable during high-resolution imaging. We also compared the PL trajectories of individual NCs before and after annealing at 100 °C with their morphology but did not find any noticeable correlation (Fig. S13 in the ESM). These results suggest that variations in morphology (i.e., core size or shell coverage) are not the dominating factor responsible for variations in PL intermittency. The distinct behaviors observed among different NCs upon annealing appear to result from the types of defects present in the NC (and their energies), which cannot be imaged using high-resolution TEM due to the sensitivity of the sample.

We prepared thin films of $CsPbBr_3@SiO_2$ NCs to understand how the variations in PL intermittency of individual NCs affect their ensemble optical properties. In previous studies, heating films of uncoated $CsPbBr_3$ NCs to temperatures between 50 °C and 100 °C led to an irreversible decrease in their PL intensity [33, 80]. Encapsulating $CsPbBr_3$ NCs in either a silica or polymer matrix provides higher temperature stability, but irreversible loss of the PL intensity is still observed at temperatures between 120 and 175 °C [31, 32, 81]. Note that the on-fraction measured by single-particle PL is a measure of the amount of time the NC spends in an emissive state rather than the total number of photons emitted by the NC. Furthermore, the NCs are far apart from each other in the single-particle measurements. While the $CsPbBr_3$ NCs are coated with a SiO_2 shell, there is the possibility of ion migration if the shell coverage is not complete for some NCs within the film. Thus, even though the average on-fraction increased by 1% after annealing at 100 °C, an overall decrease in PLQY was observed in films of $CsPbBr_3@SiO_2$ NCs annealed at this temperature. The unannealed films of $CsPbBr_3@SiO_2$ NCs had PLQYs near 4%. An annealing temperature of 70 °C led to an increase in the PL intensity of the film. Annealing at 100 °C led to a slight decrease in PL intensity, while annealing at 120 °C led to a significant decrease (Fig. S14 in the ESM).

To investigate how thermal annealing impacts the band-edge carrier dynamics at different time scales, we performed time-resolved PL and TA spectroscopies of films of $CsPbBr_3@SiO_2$ NCs. PL decay curves using TCSPC of films annealed at different temperatures are shown in Fig. 9(a). The PL decays were each fit to a sum of three exponentials with similar time constants (within error). The shortest decay constant, τ_1, is between 0.75 and 1.3 ns, the intermediate decay constant, τ_2, is between 4.3 and 5.7 ns, and the longest decay constant, τ_3, is between 23.4 and 38.8 ns for an unannealed film and films annealed at 70, 100, and 120 °C (see Fig. S15 and Table S2 in the ESM for the fits and time constants). The radiative lifetime for colloidal solutions of $CsPbBr_3$ NCs has been measured to be between 5 and 9 ns [82–84]. Similar to previous studies of $CsPbBr_3$ NCs that have sub-unity quantum yields [29, 30, 44, 85], the value of τ_3 is significantly longer than the radiative lifetime of $CsPbBr_3$ NCs. We attribute the long-time component to reversible trapping where charge carriers in shallow trap states can repopulate the band edge leading to delayed photoluminescence [86]. Furthermore, the amplitude of τ_3 decreases relative to that of τ_1 and τ_2 with increasing annealing temperature. Thus, thermal annealing appears to decrease the concentration of trap states responsible for delayed photoluminescence.

TA spectroscopy experiments were performed on an unannealed film of $CsPbBr_3@SiO_2$ NCs and a film annealed at 100 °C. The full TA data are presented in Fig. S17 in the ESM. The temporal profiles of the band-edge bleach features in the TA data, 2.441 eV for the unannealed sample and 2.419 eV for the sample after annealing at 100 °C, appear on instrument-limited timescales and decay multiexponentially. The carrier dynamics that contribute to these TA signals at short times are complicated by contributions from band-gap renormalization, intraband carrier relaxation to the band-edge states, and carrier recombination [87–94] in addition to the carrier trapping within the $CsPbBr_3@SiO_2$ NCs that is of interest for these studies. Inspection of the temporal profiles of these bleach signals indicate the contributions from band-gap renormalization and carrier relaxation become static within 4 ps after photoexcitation as the carriers have relaxed into the band-edge states by this time. Thus, we focus on the temporal decay of the band-edge bleach features for times greater than 4 ps, plotted in Fig. 9(b), even though contributions from carrier trapping are present before this time. The two band-edge bleach decay profiles were normalized at 7000 ps after photoexcitation to facilitate comparison. The two band-edge bleach decay profiles for times greater than 4 ps were fit to a sum of three exponential decays to quantify the differences (see Table S3 in the ESM for the time constants and their amplitudes). The time constant of the longest decay, τ_3, was fixed at 7500 ps, which is approximately the radiative lifetime measured for $CsPbBr_3$ NCs [82–84].

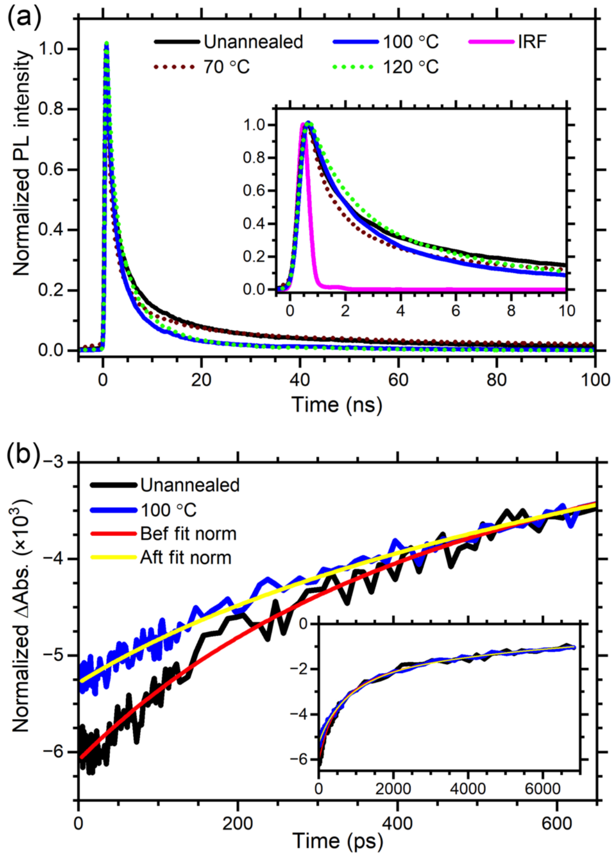

Figure 9 Time-resolved spectroscopy of films of $CsPbBr_3@SiO_2$ NCs. (a) PL decay traces from TCSPC recorded at the maximum of the PL emission band for an unannealed film (black) and films annealed at 70 °C (brown), 100 °C (blue), and 120 °C (green). To facilitate comparison, the traces are normalized at their maximum. The inset shows an expansion of the decay profiles between 0 and 10 ns. IRF = instrument response function. (b) Normalized temporal profiles of the band-edge bleach signal in the TA data. The profiles are for energies of 2.441 and 2.419 eV for an unannealed film (black) and a film annealed at 100 °C (blue), respectively. Fits to the temporal profiles are shown in red for unannealed film and yellow for the annealed film. The inset includes the same TA data, plotted out to 7000 ps, the longest time recorded and the time at which the signals were normalized.

The ΔAbs. bleach signals of the films of $CsPbBr_3@SiO_2$ NCs before and after annealing decay proportionally after a time of ~ 500 ps, see inset in Fig. 9(b). The intermediate time constant for both samples was determined to be the same within error, τ_2 ~ 830 ps. The amplitudes for the intermediate and long-time components were also found to be the same for each decay; $A_2 = 1.2(3) \times 10^{-3}$ and $A_3 = 1.28(4) \times 10^{-3}$ for the film before annealing, and $A_2 = 1.9(1) \times 10^{-3}$ and $A_3 = 1.91(3) \times 10^{-3}$ for the films after annealing. These results suggest the dynamics and radiative recombination of the carriers in the band-edge states are the same at long times. There is, however, a noticeable difference in the decay profiles at short times, < 500 ps, Fig. 9(b). The short-time decay constants are the same (within error), τ_1 = 250(80) and 150(80) ps for the films before and after annealing, but the amplitudes of the components are noticeably different. The amplitude of the short-time component decreases with annealing, making up only 5(3)% of the total amplitude after annealing in comparison to 22(13)% for the unannealed film.

Combining ensemble structural and optical characterization with single-particle PL microscopy, we propose a mechanism for the changes in on-fraction after thermal annealing depicted in Fig. 10. Etching of the $CsPbBr_3$ NCs during growth of the SiO_2 shell can promote the formation of halide vacancies on the surface of the NCs that expose lead ions. The reaction temperature of 35 °C used for shell growth is likely too low to form lead–oxygen bonds at the interface between $CsPbBr_3$ and SiO_2. Undercoordinated Pb ions are known to introduce trap states for photoexcited electrons in lead halide perovskite nanocrystals [61, 84, 95, 96]. Thermal annealing can then increase bonding at the $CsPbBr_3/SiO_2$ interface, which is reflected in the oxidation of Pb and Cs observed by XPS. The formation of interfacial Pb–O bonds passivates surface Pb ions, leading to a reduction in the density of trap states for photoexcited electrons. The decrease in the amplitude of the long-time component of the time-resolved PL spectra suggests that trap states from undercoordinated Pb are responsible for the delayed PL. While TA spectroscopy probes the dynamics of both photoexcited electrons and holes, previous work has shown that the electron dynamics contribute more to the overall TA signal in $CsPbBr_3$ NCs [97, 98]. Thus, the decrease in amplitude of the short-time decay component in the TA data reflects the passivation of surface Pb ions and corresponding reduction in the density of electron traps caused by annealing at 100 °C. Furthermore, the presence of Pb in a lower oxidation state relative to that in the $CsPbBr_3$ lattice observed by XPS before annealing is consistent with the presence of the interstitial and antisite defects, Pb_i and Pb_{Br}, which act as deep electron traps in $CsPbBr_3$ [99]. Such deep traps may be responsible for the population of NCs that exhibit type-A blinking. Oxidation of Cs and Pb at the interface with the SiO_2 shell during annealing extracts these ions from the interior of the nanocrystal due to their high ionic mobility. Thus, annealing removes Pb_i and Pb_{Br} defects but can also promote the formation of vacancy defects, V_{Cs}, and V_{Pb}, which are shallow hole traps in $CsPbBr_3$ [99]. The new vacancy defects can, in turn, lead to the decrease in on-fraction observed for a portion of the $CsPbBr_3@SiO_2$ NCs and the overall decrease in PLQY for films annealed at 100 and 120 °C. These competing processes, i.e., removal of electron traps (Pb_i, Pb_{Br}, and undercoordinated surface Pb ions) and creation of hole traps (V_{Cs}, and V_{Pb}) (Fig. 10) will occur to varying extents among the population of nanocrystals. Thus, at the single-particle level, some $CsPbBr_3@SiO_2$ NCs exhibit an increase in their on-fraction while other exhibit a decrease, leading to a wide distribution in the changes in on-fraction (Fig. 5). The rates of these competing processes also depend on the annealing temperature. For annealing at 100 °C, nearly equal numbers of NCs exhibit an increase vs. decrease in their on-fraction. However, for annealing at 120 °C, the creation of new trap states outweighs the healing of pre-existing ones, such that the majority of NCs exhibit a decrease in their on-fraction, and a substantial loss in PL intensity is observed for the film annealed at this temperature.

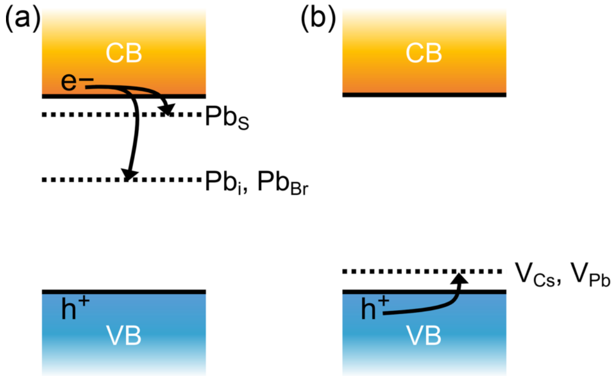

Figure 10 Schematic showing changes in the types of trap states present in $CsPbBr_3@SiO_2$ NCs before and after thermal annealing. (a) Defects that act as shallow traps (undercoordinated surface Pb ions, Pb_S) and deep traps (interstitial Pb ions, Pb_i, and antisite substitution of Pb for Br, Pb_{Br}) for photoexcited electrons are present in the initial $CsPbBr_3@SiO_2$ NCs. (b) Thermal annealing tends to passivate these electron traps but also introduces cesium and lead vacancies (V_{Cs} and V_{Pb}) that acts as shallow traps for photoexcited holes.

4 Conclusions

Single-particle microscopy reveals information that is hidden among the ensemble of nanocrystals. Thermal annealing produces a wide distribution in the change in on-fraction for individual NCs from the same synthetic batch. $CsPbBr_3@SiO_2$ NCs with initially high trap densities (i.e., that blink more frequently) are more likely to exhibit an increase in their on-fraction after annealing at 100 °C, while those with initially longer on periods are more likely to have a decrease in their on-fraction. Based on X-ray photoelectron, time-resolved PL, and TA spectroscopies performed on thin films, we attribute these differences in behavior to heterogeneity in the trap states initially present in the nanocrystals. The formation of Pb–O bonds at the $CsPbBr_3/SiO_2$ interface when heating the NCs can passivate electron traps from undercoordinated Pb ions while simultaneously introducing vacancy defects that act as shallow hole traps. This work provides insights into how trap states in individual semiconductor NCs are affected by elevated temperatures. Such effects are important to consider when optimizing the performance of optoelectronic devices that incorporate lead halide perovskite NCs. While there have been significant advances in passivating electron trap states due to undercoordinated surface Pb ions [95], our results indicate it will also be important to develop strategies that prevent the formation of hole traps when lead halide perovskite nanocrystals are exposed to elevated temperatures.

Acknowledgements

This material is based upon work supported by the National Science Foundation (NSF) under grant No. CHE-1753344 to B. S. and grant No. DMR-1905751 to R. A. L. D. M. N. acknowledges the Center for Solar Energy and Energy Storage at the McKelvey School of Engineering at Washington University in Saint Louis for financial support. Electron microscopy and X-ray photoelectron spectroscopy were performed at the Institute of Materials Science & Engineering at Washington University. X-ray diffraction was performed in the Department of Earth, Environmental, and Planetary Sciences at Washington University.

Electronic Supplementary Material: Supplementary material (experimental details on the synthesis of silica microspheres, correlative photoluminescence microscopy and transmission electron microscopy, X-ray diffraction, and photoluminescence quantum yields; supplementary tables providing fits to the X-ray photoelectron spectra, time-resolved PL spectra, and transient absorption spectra; supplementary figures showing optical spectra of the precipitate and supernatant of $CsPbBr_3@SiO_2$ nanocrystals, XRD patterns, size histograms, XPS data, PL intensity trajectories after annealing, on-fractions before and after annealing, probability distributions of on-events and slopes of the power-law fitting, correlative TEM and PL microscopy, extinction and PL spectra of films before and after annealing, fits to the time-resolved PL spectra, and TA data) is available in the online version of this article at https://doi.org/10.1007/s12274-024-6989-3.

References

[1] Green, M. A.; Ho-Baillie, A.; Snaith, H. J. The emergence of perovskite solar cells. *Nat. Photonics* **2014**, *8*, 506–514.

[2] Protesescu, L.; Yakunin, S.; Bodnarchuk, M. I.; Krieg, F.; Caputo, R.; Hendon, C. H.; Yang, R. X.; Walsh, A.; Kovalenko, M. V. Nanocrystals of cesium lead halide perovskites ($CsPbX_3$, X = Cl, Br, and I): Novel optoelectronic materials showing bright emission with wide color gamut. *Nano Lett.* **2015**, *15*, 3692–3696.

[3] Kovalenko, M. V.; Protesescu, L.; Bodnarchuk, M. I. Properties and potential optoelectronic applications of lead halide perovskite nanocrystals. *Science* **2017**, *358*, 745–750.

[4] Li, X. M.; Cao, F.; Yu, D. J.; Chen, J.; Sun, Z. G.; Shen, Y. L.; Zhu, Y.; Wang, L.; Wei, Y.; Wu, Y. et al. All inorganic halide perovskites nanosystem: Synthesis, structural features, optical properties and optoelectronic applications. *Small* **2017**, *13*, 1603996.

[5] Rainò, G.; Becker, M. A.; Bodnarchuk, M. I.; Mahrt, R. F.; Kovalenko, M. V.; Stöferle, T. Superfluorescence from lead halide perovskite quantum dot superlattices. *Nature* **2018**, *563*, 671–675.

[6] Akkerman, Q. A.; Abdelhady, A. L.; Manna, L. Zero-dimensional cesium lead halides: History, properties, and challenges. *J. Phys. Chem. Lett.* **2018**, *9*, 2326–2337.

[7] Utzat, H.; Sun, W. W.; Kaplan, A. E. K.; Krieg, F.; Ginterseder, M.; Spokoyny, B.; Klein, N. D.; Shulenberger, K. E.; Perkinson, C. F.; Kovalenko, M. V. et al. Coherent single-photon emission from colloidal lead halide perovskite quantum dots. *Science* **2019**, *363*, 1068–1072.

[8] Deschler, F.; Neher, D.; Schmidt-Mende, L. Perovskite

semiconductors for next generation optoelectronic applications. *APL Mater.* **2019**, *7*, 080401.

[9] Fu, Y. P.; Zhu, H. M.; Chen, J.; Hautzinger, M. P.; Zhu, X. Y.; Jin, S. Metal halide perovskite nanostructures for optoelectronic applications and the study of physical properties. *Nat. Rev. Mater.* **2019**, *4*, 169–188.

[10] Chouhan, L.; Ghimire, S.; Subrahmanyam, C.; Miyasaka, T.; Biju, V. Synthesis, optoelectronic properties and applications of halide perovskites. *Chem. Soc. Rev.* **2020**, *49*, 2869–2885.

[11] Leijtens, T.; Eperon, G. E.; Noel, N. K.; Habisreutinger, S. N.; Petrozza, A.; Snaith, H. J. Stability of metal halide perovskite solar cells. *Adv. Energy Mater.* **2015**, *5*, 1500963.

[12] Wang, D.; Wright, M.; Elumalai, N. K.; Uddin, A. Stability of perovskite solar cells. *Solar Energy Mater. Solar Cells* **2016**, *147*, 255–275.

[13] Meng, L.; You, J. B.; Yang, Y. Addressing the stability issue of perovskite solar cells for commercial applications. *Nat. Commun.* **2018**, *9*, 5265.

[14] Ling, J.; Kizhakkedath, P. K. K.; Watson, T. M.; Mora-Seró, I.; Schmidt-Mende, L.; Brown, T. M.; Jose, R. A perspective on the commercial viability of perovskite solar cells. *Sol. RRL* **2021**, *5*, 2100401.

[15] Chowdhury, T. A.; Bin Zafar, M. A.; Sajjad-Ul Islam, M.; Shahinuzzaman, M.; Islam, M. A.; Khandaker, M. U. Stability of perovskite solar cells: Issues and prospects. *RSC Adv.* **2023**, *13*, 1787–1810.

[16] Yang, J. L.; Siempelkamp, B. D.; Liu, D. Y.; Kelly, T. L. Investigation of $CH_3NH_3PbI_3$ degradation rates and mechanisms in controlled humidity environments using *in situ* techniques. *ACS Nano* **2015**, *9*, 1955–1963.

[17] Bryant, D.; Aristidou, N.; Pont, S.; Sanchez-Molina, I.; Chotchunangatchaval, T.; Wheeler, S.; Durrant, J. R.; Haque, S. A. Light and oxygen induced degradation limits the operational stability of methylammonium lead triiodide perovskite solar cells. *Energy Environ. Sci.* **2016**, *9*, 1655–1660.

[18] Pearson, A. J.; Eperon, G. E.; Hopkinson, P. E.; Habisreutinger, S. N.; Wang, J. T. W.; Snaith, H. J.; Greenham, N. C. Oxygen degradation in mesoporous $Al_2O_3/CH_3NH_3PbI_{3-x}Cl_x$ perovskite solar cells: Kinetics and mechanisms. *Adv. Energy Mater.* **2016**, *6*, 1600014.

[19] Juarez-Perez, E. J.; Hawash, Z.; Raga, S. R.; Ono, L. K.; Qi, Y. B. Thermal degradation of $CH_3NH_3PbI_3$ perovskite into NH_3 and CH_3I gases observed by coupled thermogravimetry-mass spectrometry analysis. *Energy Environ. Sci.* **2016**, *9*, 3406–3410.

[20] Meng, Q.; Chen, Y. C.; Xiao, Y. Y.; Sun, J. J.; Zhang, X. B.; Han, C. B.; Gao, H. L.; Zhang, Y. Z.; Yan, H. Effect of temperature on the performance of perovskite solar cells. *J. Mater. Sci. Mater. Electron.* **2021**, *32*, 12784–12792.

[21] Abdelmageed, G.; Jewell, L.; Hellier, K.; Seymour, L.; Luo, B. B.; Bridges, F.; Zhang, J. Z.; Carter, S. Mechanisms for light induced degradation in $MAPbI_3$ perovskite thin films and solar cells. *Appl. Phys. Lett.* **2016**, *109*, 233905.

[22] Draguta, S.; Sharia, O.; Yoon, S. J.; Brennan, M. C.; Morozov, Y. V.; Manser, J. S.; Kamat, P. V.; Schneider, W. F.; Kuno, M. Rationalizing the light-induced phase separation of mixed halide organic-inorganic perovskites. *Nat. Commun.* **2017**, *8*, 200.

[23] Nickel, N. H.; Lang, F.; Brus, V. V.; Shargaieva, O.; Rappich, J. Unraveling the light-induced degradation mechanisms of $CH_3NH_3PbI_3$ perovskite films. *Adv. Electron. Mater.* **2017**, *3*, 1700158.

[24] Song, Z. N.; Wang, C. L.; Phillips, A. B.; Grice, C. R.; Zhao, D. W.; Yu, Y.; Chen, C.; Li, C. W.; Yin, X. X.; Ellingson, R. J. et al. Probing the origins of photodegradation in organic-inorganic metal halide perovskites with time-resolved mass spectrometry. *Sustain. Energy Fuels* **2018**, *2*, 2460–2467.

[25] Swarnkar, A.; Marshall, A. R.; Sanehira, E. M.; Chernomordik, B. D.; Moore, D. T.; Christians, J. A.; Chakrabarti, T.; Luther, J. M. Quantum dot-induced phase stabilization of α-$CsPbI_3$ perovskite for high-efficiency photovoltaics. *Science* **2016**, *354*, 92–95.

[26] Kulbak, M.; Gupta, S.; Kedem, N.; Levine, I.; Bendikov, T.; Hodes, G.; Cahen, D. Cesium enhances long-term stability of lead bromide perovskite-based solar cells. *J. Phys. Chem. Lett.* **2016**, *7*, 167–172.

[27] Shangguan, Z. B.; Zheng, X.; Zhang, J.; Lin, W. S.; Guo, W. J.; Li, C.; Wu, T. Z.; Lin, Y.; Chen, Z. The stability of metal halide perovskite nanocrystals-a key issue for the application on quantum-dot-based micro light-emitting diodes display. *Nanomaterials* **2020**, *10*, 1375.

[28] Zhong, Q. X.; Cao, M. H.; Hu, H. C.; Yang, D.; Chen, M.; Li, P. L.; Wu, L. Z.; Zhang, Q. One-pot synthesis of highly stable $CsPbBr_3@SiO_2$ core–shell nanoparticles. *ACS Nano* **2018**, *12*, 8579–8587.

[29] Hu, H. C.; Wu, L. Z.; Tan, Y. S.; Zhong, Q. X.; Chen, M.; Qiu, Y. H.; Yang, D.; Sun, B. Q.; Zhang, Q.; Yin, Y. D. Interfacial synthesis of highly stable $CsPbX_3$/oxide Janus nanoparticles. *J. Am. Chem. Soc.* **2018**, *140*, 406–412.

[30] Wang, Y. N.; Dong, Y. J.; Liu, Q.; Guo, X.; Zhang, M. J.; Li, Y. F. *In-situ* stabilization strategy for $CsPbX_3$-silicone resin composite with enhanced luminescence and stability. *Nano Energy* **2020**, *78*, 105150.

[31] Gao, F.; Yang, W. Q.; Liu, X. L.; Li, Y. Z.; Liu, W. Z.; Xu, H. Y.; Liu, Y. C. Highly stable and luminescent silica-coated perovskite quantum dots at nanoscale-particle level via nonpolar solvent synthesis. *Chem. Eng. J.* **2021**, *407*, 128001.

[32] Diroll, B. T.; Nedelcu, G.; Kovalenko, M. V.; Schaller, R. D. High-temperature photoluminescence of $CsPbX_3$ (X = Cl, Br, I) nanocrystals. *Adv. Funct. Mater.* **2017**, *27*, 1606750.

[33] Yuan, X.; Hou, X. M.; Li, J.; Qu, C. Q.; Zhang, W. J.; Zhao, J. L.; Li, H. B. Thermal degradation of luminescence in inorganic perovskite $CsPbBr_3$ nanocrystals. *Phys. Chem. Chem. Phys.* **2017**, *19*, 8934–8940.

[34] Wang, Q.; Wu, W. Z.; Wu, R. R.; Yang, S.; Wang, Y. X.; Wang, J. X.; Chai, Z. J.; Han, Q. J. Improved thermal stability of photoluminescence in Cs_4PbBr_6 microcrystals/$CsPbBr_3$ nanocrystals. *J. Colloid Interface Sci.* **2019**, *554*, 133–141.

[35] Huang, S. Q.; Li, Z. C.; Wang, B.; Zhu, N. W.; Zhang, C. Y.; Kong, L.; Zhang, Q.; Shan, A. D.; Li, L. Morphology evolution and degradation of $CsPbBr_3$ nanocrystals under blue light-emitting diode illumination. *ACS Appl. Mater. Interfaces* **2017**, *9*, 7249–7258.

[36] An, R.; Zhang, F. Y.; Zou, X. S.; Tang, Y. Y.; Liang, M. L.; Oshchapovskyy, I.; Liu, Y. C.; Honarfar, A.; Zhong, Y. Q.; Li, C. S. et al. Photostability and photodegradation processes in colloidal $CsPbI_3$ perovskite quantum dots. *ACS Appl. Mater. Interfaces* **2018**, *10*, 39222–39227.

[37] Scheidt, R. A.; Kerns, E.; Kamat, P. V. Interfacial charge transfer between excited $CsPbBr_3$ nanocrystals and TiO_2: Charge injection versus photodegradation. *J. Phys. Chem. Lett.* **2018**, *9*, 5962–5969.

[38] Boote, B. W.; Andaraarachchi, H. P.; Rosales, B. A.; Blome-Fernández, R.; Zhu, F.; Reichert, M. D.; Santra, K.; Li, J. Z.; Petrich, J. W.; Vela, J. et al. Unveiling the photo- and thermal-stability of cesium lead halide perovskite nanocrystals. *ChemPhysChem* **2019**, *20*, 2647–2656.

[39] Yuan, G. C.; Ritchie, C.; Ritter, M.; Murphy, S.; Gómez, D. E.; Mulvaney, P. The degradation and blinking of single $CsPbI_3$ perovskite quantum dots. *J. Phys. Chem. C* **2018**, *122*, 13407–13415.

[40] Liu, L. G.; Deng, L. G.; Huang, S.; Zhang, P.; Linnros, J.; Zhong, H. Z.; Sychugov, I. Photodegradation of organometal hybrid perovskite nanocrystals: Clarifying the role of oxygen by single-dot photoluminescence. *J. Phys. Chem. Lett.* **2019**, *10*, 864–869.

[41] Zhang, C.; Fernando, J. F. S.; Firestein, K. L.; von Treifeldt, J. E.; Siriwardena, D.; Fang, X. S.; Golberg, D. Thermal stability of $CsPbBr_3$ perovskite as revealed by *in situ* transmission electron microscopy. *APL Mater.* **2019**, *7*, 071110.

[42] Matteocci, F.; Cinà, L.; Lamanna, E.; Cacovich, S.; Divitini, G.; Midgley, P. A.; Ducati, C.; Di Carlo, A. Encapsulation for long-term stability enhancement of perovskite solar cells. *Nano Energy* **2016**, *30*, 162–172.

[43] Dipta, S. S.; Rahim, A.; Uddin, A. Encapsulating perovskite solar cells for long-term stability and prevention of lead toxicity. *Appl. Phys. Rev.* **2024**, *11*, 021301.

[44] Liao, J. F.; Xu, Y. F.; Wang, X. D.; Chen, H. Y.; Kuang, D. B.

CsPbBr$_3$ nanocrystal/MO$_2$ (M = Si, Ti, Sn) composites: Insight into charge-carrier dynamics and photoelectrochemical applications. *ACS Appl. Mater. Interfaces* **2018**, *10*, 42301–42309.

[45] Dubey, S.; Sarvaiya, J. N.; Seshadri, B. Temperature dependent photovoltaic (PV) efficiency and its effect on PV production in the world-a review. *Energy Procedia* **2013**, *33*, 311–321.

[46] Kim, D. Y.; Park, J.; Cho, J.; Kim, J. K. Counter-intuitive junction temperature behavior in AlGaN-based deep-ultraviolet light-emitting diodes. *AIP Adv.* **2020**, *10*, 045135.

[47] Liu, M. M.; Wan, Q.; Wang, H. M.; Carulli, F.; Sun, X. C.; Zheng, W. L.; Kong, L.; Zhang, Q.; Zhang, C. Y.; Zhang, Q. G. et al. Suppression of temperature quenching in perovskite nanocrystals for efficient and thermally stable light-emitting diodes. *Nat. Photonics* **2021**, *15*, 379–385.

[48] Routzahn, A. L.; Jain, P. K. Single-nanocrystal reaction trajectories reveal sharp cooperative transitions. *Nano Lett.* **2014**, *14*, 987–992.

[49] Yoshimura, H.; Yamauchi, M.; Masuo, S. *In situ* observation of emission behavior during anion-exchange reaction of a cesium lead halide perovskite nanocrystal at the single-nanocrystal level. *J. Phys. Chem. Lett.* **2020**, *11*, 530–535.

[50] Wang, D.; Cavin, J.; Yin, B.; Thind, A. S.; Borisevich, A. Y.; Mishra, R.; Sadtler, B. Role of solid-state miscibility during anion exchange in cesium lead halide nanocrystals probed by single-particle fluorescence. *J. Phys. Chem. Lett.* **2020**, *11*, 952–959.

[51] Wang, D.; Zhang, D. Y.; Sadtler, B. Irreversibility in anion exchange between cesium lead bromide and iodide nanocrystals imaged by single-particle fluorescence. *J. Phys. Chem. C* **2020**, *124*, 27158–27168.

[52] Karimata, I.; Tachikawa, T. *In situ* exploration of the structural transition during morphology- and efficiency-conserving halide exchange on a single perovskite nanocrystal. *Angew. Chem., Int. Ed.* **2021**, *60*, 2548–2553.

[53] Zhang, D. Y.; Wu, X. S.; Wang, D.; Sadtler, B. Size-dependent miscibility controls the kinetics of anion exchange in cesium lead halide nanocrystals. *J. Chem. Phys.* **2023**, *159*, 014701.

[54] Nirmal, M.; Dabbousi, B. O.; Bawendi, M. G.; Macklin, J. J.; Trautman, J. K.; Harris, T. D.; Brus, L. E. Fluorescence intermittency in single cadmium selenide nanocrystals. *Nature* **1996**, *383*, 802–804.

[55] Shimizu, K. T.; Neuhauser, R. G.; Leatherdale, C. A.; Empedocles, S. A.; Woo, W. K.; Bawendi, M. G. Blinking statistics in single semiconductor nanocrystal quantum dots. *Phys. Rev. B* **2001**, *63*, 205316.

[56] Kuno, M.; Fromm, D. P.; Hamann, H. F.; Gallagher, A.; Nesbitt, D. J. "On"/"off" fluorescence intermittency of single semiconductor quantum dots. *J. Chem. Phys.* **2001**, *115*, 1028–1040.

[57] Kuno, M.; Fromm, D. P.; Johnson, S. T.; Gallagher, A.; Nesbitt, D. J. Modeling distributed kinetics in isolated semiconductor quantum dots. *Phys. Rev. B* **2003**, *67*, 125304.

[58] Zhao, J.; Nair, G.; Fisher, B. R.; Bawendi, M. G. Challenge to the charging model of semiconductor-nanocrystal fluorescence intermittency from off-state quantum yields and multiexciton blinking. *Phys. Rev. Lett.* **2010**, *104*, 157403.

[59] Galland, C.; Ghosh, Y.; Steinbrück, A.; Sykora, M.; Hollingsworth, J. A.; Klimov, V. I.; Htoon, H. Two types of luminescence blinking revealed by spectroelectrochemistry of single quantum dots. *Nature* **2011**, *479*, 203–207.

[60] Park, Y. S.; Guo, S. J.; Makarov, N. S.; Klimov, V. I. Room temperature single-photon emission from individual perovskite quantum dots. *ACS Nano* **2015**, *9*, 10386–10393.

[61] Tachikawa, T.; Karimata, I.; Kobori, Y. Surface charge trapping in organolead halide perovskites explored by single-particle photoluminescence imaging. *J. Phys. Chem. Lett.* **2015**, *6*, 3195–3201.

[62] Rainò, G.; Nedelcu, G.; Protesescu, L.; Bodnarchuk, M. I.; Kovalenko, M. V.; Mahrt, R. F.; Stöferle, T. Single cesium lead halide perovskite nanocrystals at low temperature: Fast single-photon emission, reduced blinking, and exciton fine structure. *ACS Nano* **2016**, *10*, 2485–2490.

[63] Gibson, N. A.; Koscher, B. A.; Alivisatos, A. P.; Leone, S. R. Excitation intensity dependence of photoluminescence blinking in CsPbBr$_3$ perovskite nanocrystals. *J. Phys. Chem. C* **2018**, *122*, 12106–12113.

[64] Trinh, C. T.; Minh, D. N.; Ahn, K. J.; Kang, Y.; Lee, K. G. Organic-inorganic FAPbBr$_3$ perovskite quantum dots as a quantum light source: Single-photon emission and blinking behaviors. *ACS Photonics* **2018**, *5*, 4937–4943.

[65] Freppon, D. J.; Men, L.; Burkhow, S. J.; Petrich, J. W.; Vela, J.; Smith, E. A. Photophysical properties of wavelength-tunable methylammonium lead halide perovskite nanocrystals. *J. Mater. Chem. C* **2017**, *5*, 118–126.

[66] Seth, S.; Ahmed, T.; Samanta, A. Photoluminescence flickering and blinking of single CsPbBr$_3$ perovskite nanocrystals: Revealing explicit carrier recombination dynamics. *J. Phys. Chem. Lett.* **2018**, *9*, 7007–7014.

[67] Ahmed, T.; Seth, S.; Samanta, A. Mechanistic investigation of the defect activity contributing to the photoluminescence blinking of CsPbBr$_3$ perovskite nanocrystals. *ACS Nano* **2019**, *13*, 13537–13544.

[68] Yang, C. G.; Li, Y.; Hou, X. Q.; Zhang, M.; Zhang, G. F.; Li, B.; Guo, W. L.; Han, X.; Bai, X. Q.; Li, J. L. et al. Conversion of photoluminescence blinking types in single colloidal quantum dots. *Small* **2024**, *20*, 2309134.

[69] Sanderson, W. M.; Schrier, J.; Loomis, R. A. Photo-induced state shifting in 1D semiconductor quantum wires. *J. Phys. Chem. C* **2020**, *124*, 16702–16713.

[70] Mannino, G.; Deretzis, I.; Smecca, E.; La Magna, A.; Alberti, A.; Ceratti, D.; Cahen, D. Temperature-dependent optical band gap in CsPbBr$_3$, MAPbBr$_3$, and FAPbBr$_3$ single crystals. *J. Phys. Chem. Lett.* **2020**, *11*, 2490–2496.

[71] Shen, M. K.; Ding, T. B.; Luo, J.; Tan, C.; Mahmood, K.; Wang, Z. Y.; Zhang, D. Y.; Mishra, R.; Lew, M. D.; Sadtler, B. Competing activation and deactivation mechanisms in photodoped bismuth oxybromide nanoplates probed by single-molecule fluorescence imaging. *J. Phys. Chem. Lett.* **2020**, *11*, 5219–5227.

[72] Zhao, Z. Y.; Xu, W.; Pan, G. C.; Liu, Y. A.; Yang, M.; Hua, S. W.; Chen, X.; Peng, H. S.; Song, H. W. Enhancing the exciton emission of CsPbCl$_3$ perovskite quantum dots by incorporation of Rb$^+$ ions. *Mater. Res. Bull.* **2019**, *112*, 142–146.

[73] van Sark, W. G. J. H. M.; Frederix, P. L. T. M.; Van den Heuvel, D. J.; Gerritsen, H. C.; Bol, A. A.; van Lingen, J. N. J.; de Mello Donegá, C.; Meijerink, A. Photooxidation and photobleaching of single CdSe/ZnS quantum dots probed by room-temperature time-resolved spectroscopy. *J. Phys. Chem. B* **2001**, *105*, 8281–8284.

[74] Manna, L.; Scher, E. C.; Li, L. S.; Alivisatos, A. P. Epitaxial growth and photochemical annealing of graded CdS/ZnS shells on colloidal CdSe nanorods. *J. Am. Chem. Soc.* **2002**, *124*, 7136–7145.

[75] Carrillo-Carrión, C.; Cárdenas, S.; Simonet, B. M.; Valcárcel, M. Quantum dots luminescence enhancement due to illumination with UV/Vis light. *Chem. Commun.* **2009**, 5214–5226.

[76] Dang, Z. Y.; Shamsi, J.; Palazon, F.; Imran, M.; Akkerman, Q. A.; Park, S.; Bertoni, G.; Prato, M.; Brescia, R.; Manna, L. *In situ* transmission electron microscopy study of electron beam-induced transformations in colloidal cesium lead halide perovskite nanocrystals. *ACS Nano* **2017**, *11*, 2124–2132.

[77] Liu, W. N.; Zheng, J. J.; Shang, M. H.; Fang, Z.; Chou, K. C.; Yang, W. Y.; Hou, X. M.; Wu, T. Electron-beam irradiation-hard metal-halide perovskite nanocrystals. *J. Mater. Chem. A* **2019**, *7*, 10912–10917.

[78] Ran, J. H.; Dyck, O.; Wang, X. Z.; Yang, B.; Geohegan, D. B.; Xiao, K. Electron-beam-related studies of halide perovskites: Challenges and opportunities. *Adv. Energy Mater.* **2020**, *10*, 1903191.

[79] Orfield, N. J.; McBride, J. R.; Keene, J. D.; Davis, L. M.; Rosenthal, S. J. Correlation of atomic structure and photoluminescence of the same quantum dot: Pinpointing surface and internal defects that inhibit photoluminescence. *ACS Nano* **2015**, *9*, 831–839.

[80] Wei, S.; Yang, Y. C.; Kang, X. J.; Wang, L.; Huang, L. J.; Pan, D. C. Room-temperature and gram-scale synthesis of CsPbX$_3$ (X = Cl, Br, I) perovskite nanocrystals with 50-85% photoluminescence quantum yields. *Chem. Commun.* **2016**, *52*, 7265–7268.

[81] Liang, P. T.; Zhang, P.; Pan, A. Z.; Yan, K.; Zhu, Y. S.; Yang, M.

Y.; He, L. Unusual stability and temperature-dependent properties of highly emissive $CsPbBr_3$ perovskite nanocrystals obtained from *in situ* crystallization in poly(vinylidene difluoride). *ACS Appl. Mater. Interfaces* **2019**, *11*, 22786–22793.

[82] Utzat, H.; Shulenberger, K. E.; Achorn, O. B.; Nasilowski, M.; Sinclair, T. S.; Bawendi, M. G. Probing linewidths and biexciton quantum yields of single cesium lead halide nanocrystals in solution. *Nano Lett.* **2017**, *17*, 6838–6846.

[83] Makarov, N. S.; Guo, S. J.; Isaienko, O.; Liu, W. Y.; Robel, I.; Klimov, V. I. Spectral and dynamical properties of single excitons, biexcitons, and trions in cesium-lead-halide perovskite quantum dots. *Nano Lett.* **2016**, *16*, 2349–2362.

[84] Koscher, B. A.; Swabeck, J. K.; Bronstein, N. D.; Alivisatos, A. P. Essentially trap-free $CsPbBr_3$ colloidal nanocrystals by postsynthetic thiocyanate surface treatment. *J. Am. Chem. Soc.* **2017**, *139*, 6566–6569.

[85] Di Stasio, F.; Christodoulou, S.; Huo, N. J.; Konstantatos, G. Near-unity photoluminescence quantum yield in $CsPbBr_3$ nanocrystal solid-state films via postsynthesis treatment with lead bromide. *Chem. Mater.* **2017**, *29*, 7663–7667.

[86] Whitham, P. J.; Knowles, K. E.; Reid, P. J.; Gamelin, D. R. Photoluminescence blinking and reversible electron trapping in copper-doped CdSe nanocrystals. *Nano Lett.* **2015**, *15*, 4045–4051.

[87] Seiler, H.; Palato, S.; Sonnichsen, C.; Baker, H.; Socie, E.; Strandell, D. P.; Kambhampati, P. Two-dimensional electronic spectroscopy reveals liquid-like lineshape dynamics in $CsPbI_3$ perovskite nanocrystals. *Nat. Commun.* **2019**, *10*, 4962.

[88] Brosseau, P.; Ghosh, A.; Seiler, H.; Strandell, D.; Kambhampati, P. Exciton-polaron interactions in metal halide perovskite nanocrystals revealed via two-dimensional electronic spectroscopy. *J. Chem. Phys.* **2023**, *159*, 184711.

[89] Thouin, F.; Valverde-Chávez, D. A.; Quarti, C.; Cortecchia, D.; Bargigia, I.; Beljonne, D.; Petrozza, A.; Silva, C.; Srimath Kandada, A. R. Phonon coherences reveal the polaronic character of excitons in two-dimensional lead halide perovskites. *Nat. Mater.* **2019**, *18*, 349–356.

[90] Thouin, F.; Srimath Kandada, A. R.; Valverde-Chávez, D. A.; Cortecchia, D.; Bargigia, I.; Petrozza, A.; Yang, X. M.; Bittner, E. R.; Silva, C. Electron-phonon couplings inherent in polarons drive exciton dynamics in two-dimensional metal-halide perovskites. *Chem. Mater.* **2019**, *31*, 7085–7091.

[91] Shrivastava, M.; Hazarika, A.; Aneesh, J.; Mandal, D.; Beard, M. C.; Adarsh, K. V. Giant spin-selective bandgap renormalization in $CsPbBr_3$ colloidal nanocrystals. *Phys. Rev. B* **2022**, *106*, L041404.

[92] Yan, J. F.; Jiang, T. R.; Liu, Q. B.; Xiao, Z. J.; Zhang, W.; Zhou, H.; Wu, G. H.; Chen, Z. F. Giant band-gap renormalization and morphology-tunable defect-assisted carrier recombination in $CsPbBr_3$ microstructures. *ACS Photonics* **2023**, *10*, 3976–3984.

[93] Saran, R.; Heuer-Jungemann, A.; Kanaras, A. G.; Curry, R. J. Giant bandgap renormalization and exciton-phonon scattering in perovskite nanocrystals. *Adv. Opt. Mater.* **2017**, *5*, 1700231.

[94] Ren, Y. J.; Huang, Z. G.; Wang, Y. Dynamic and giant bandgap renormalization dictates the transient optical response in perovskite quantum dots. *Appl. Phys. Lett.* **2022**, *121*, 251103.

[95] Nenon, D. P.; Pressler, K.; Kang, J.; Koscher, B. A.; Olshansky, J. H.; Osowiecki, W. T.; Koc, M. A.; Wang, L. W.; Alivisatos, A. P. Design principles for trap-free $CsPbX_3$ nanocrystals: Enumerating and eliminating surface halide vacancies with softer Lewis bases. *J. Am. Chem. Soc.* **2018**, *140*, 17760–17772.

[96] Socie, E.; Vale, B. R. C.; Burgos-Caminal, A.; Moser, J. E. Direct observation of shallow trap states in thermal equilibrium with band-edge excitons in strongly confined $CsPbBr_3$ perovskite nanoplatelets. *Adv. Opt. Mater.* **2021**, *9*, 2001308.

[97] Wu, K. F.; Liang, G. J.; Shang, Q. Y.; Ren, Y. P.; Kong, D. G.; Lian, T. Q. Ultrafast interfacial electron and hole transfer from $CsPbBr_3$ perovskite quantum dots. *J. Am. Chem. Soc.* **2015**, *137*, 12792–12795.

[98] Mondal, N.; Samanta, A. Complete ultrafast charge carrier dynamics in photo-excited all-inorganic perovskite nanocrystals ($CsPbX_3$). *Nanoscale* **2017**, *9*, 1878–1885.

[99] Kang, J.; Wang, L. W. High defect tolerance in lead halide perovskite $CsPbBr_3$. *J. Phys. Chem. Lett.* **2017**, *8*, 489–493.